

Chapter XX:

Time-Resolved X-ray Scattering of Excited State Structure and Dynamics

Haiwang Yong^{a,†}, Adam Kirrander^b, and Peter M. Weber^{a*}

^aDepartment of Chemistry, Brown University, Providence, Rhode Island 02912, USA,

^bEaStCHEM School of Chemistry and Centre for Science at Extreme Conditions, University of Edinburgh, David Brewster Road, Edinburgh EH9 3FJ, United Kingdom

[†]Present address: Department of Chemistry, University of California, Irvine, California 92697, USA

*Corresponding email address: peter_weber@brown.edu

ABSTRACT

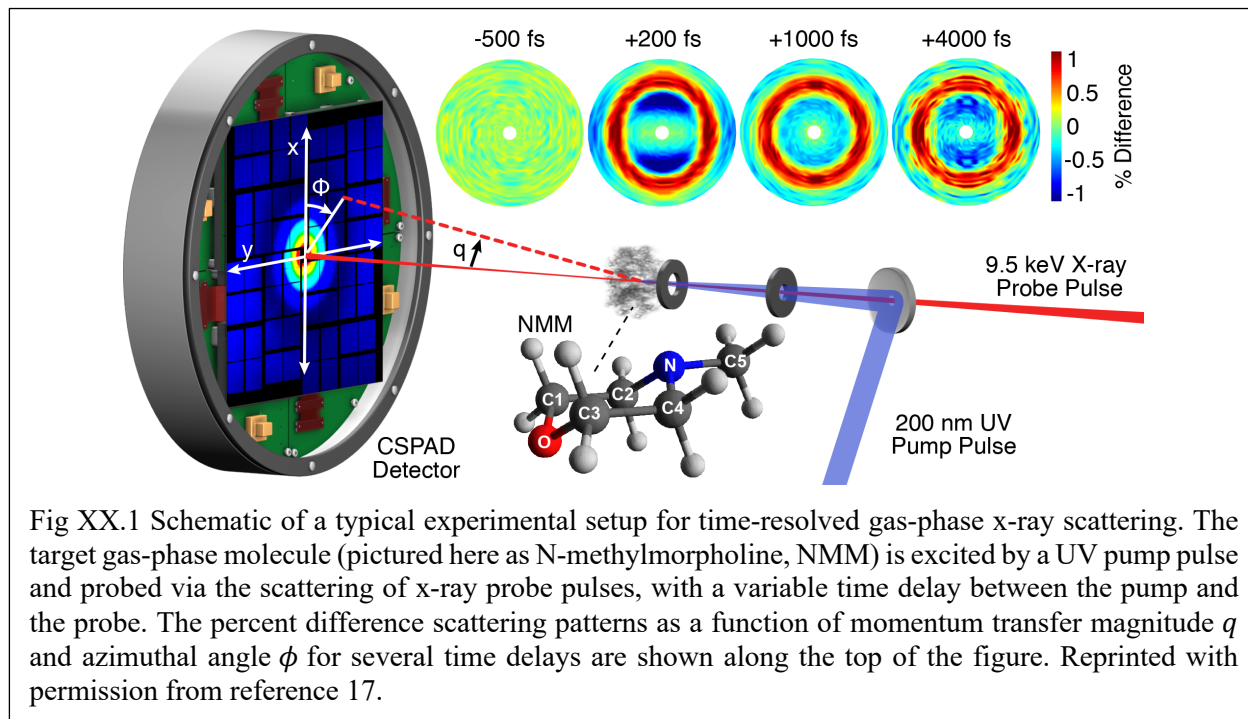
Ultrafast gas-phase x-ray scattering using x-ray free-electron lasers (XFELs) has enabled the measurement of molecular structures and dynamics in excited states with atomic spatial and femtosecond time resolution. This chapter reviews important recent advances, notably additional observables such as the orientation of optical transition dipoles within the molecular frame, excited-state molecular electron densities, and rate constants for chemical kinetics. In excited states, the structures of medium sized molecules (up to 8 non-hydrogenic atoms) have been determined with high precisions in the non-hydrogenic atom-atom distances. Effects arising from the redistribution of electron density upon optical excitation are observed and confirmed by high-level calculations, allowing for the observation of ultrafast excited state charge transfer reactions. Fragmentation of molecules is readily observed, and identifiable by a characteristic decrease in the x-ray scattering signal at small scattering angles. Furthermore, the structures of transient radical fragments have been measured.

XX.1. Introduction

To directly observe atomic motions in molecules during chemical dynamics has long constituted one of the grand challenges in chemistry¹. The emergence of x-ray free-electron lasers (XFELs) with their ultrashort pulse durations and extreme brightness^{2,3} and the near-parallel development of ultrafast electron sources (see MeV ultrafast electron diffraction chapter), has made ultrafast scattering measurements of molecular dynamics in free gas-phase molecules possible. While chemical dynamics on ground electronic state potential energy surfaces is conceptually well understood and easier to model computationally, the fact remains that excited states play important roles in chemical processes, especially in the field of photochemistry. Molecules are often more reactive in their excited states than in the ground state because activation energies can be lower and because electronic relaxation processes can insert a great deal of internal energy into vibrational modes⁴. Additionally, excitation to excited states can induce, after rapid electronic relaxation, fast kinetic or dynamic processes on the ground electronic surface. Yet, it is challenging to directly observe the rapid molecular dynamics in excited states in real time, far away from the equilibrium, and to map the atomic motions induced by electronic excitations simultaneous atomic scale spatial and femtosecond temporal resolution are required.

X-ray scattering is sensitive to the electronic charge density whereas electron diffraction measures the total (electronic + nuclear) charge density. However, the core electrons track the nuclei closely and both x-ray and electron scattering can thus be employed toward the real-space imaging of transient molecular structures. Even though x-ray scattering has a much smaller cross section and, at the photon energies currently available, covers a smaller range of scattering angles compared to electron diffraction, the high flux and high energy x-ray pulses of XFELs make up for these shortcomings. Importantly, ultrafast x-ray scattering has achieved a better temporal resolution (~30 fs) as MeV-UED is limited by the intrinsic space-charge interactions between electrons within a pulse. This makes time-resolved x-ray scattering a unique tool for measuring ultrafast processes such as the rapid redistribution of electron density upon photoexcitation. The relative merits and strengths of the two methods have been discussed extensively^{5,6,7,8}, so that the present chapter focuses on ultrafast x-ray scattering. While important studies have investigated condensed matter⁹ and solutions¹⁰, this review focuses on samples in the gas phase. In the absence of a solvent, investigations of free molecules reveal the pure and perturbed chemical dynamics of molecular species. High quality scattering patterns can be obtained and directly and quantitatively compared to theory.

Static x-ray scattering is traditionally used as an essential tool for determining molecular structure in the ground electronic state of molecules at equilibrium¹¹. Since x-ray scattering arises from the interaction of molecular electrons with the electromagnetic field of the incoming x-rays, it is a sensitive probe of the



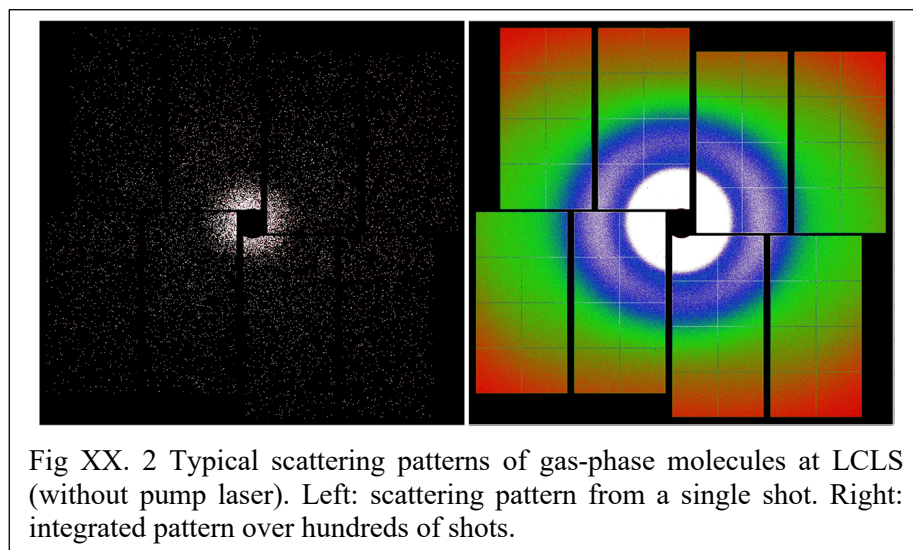
electron density distribution in a molecule. However, as mentioned above, because the atomic core electrons are usually centered tightly around the nuclei, the geometry (nuclear structure) of molecules can be determined with x-ray scattering. It is important to also mention that while time-resolved spectroscopies are fundamentally limited by the time-energy uncertainty relation, x-ray scattering does not have that limitation because it measures time and space, which are not complementary variables. Thus time-resolved x-ray scattering can, in principle, measure chemical reactions with both high spatial and temporal resolution without fundamental restrictions. All these features make ultrafast x-ray scattering a promising technique for unveiling nuclear and electron dynamics during complex chemical reactions.

The first time-resolved gas-phase x-ray scattering experiment with femtosecond time resolution was demonstrated in 2015 when a “molecular movie” of the ring-opening reaction of 1,3-cyclohexadiene (CHD) was successfully determined¹². Since then, the ultrafast gas-phase x-ray scattering setup has been developed^{13,14}, resulting in many new and previously unattainable insights about excited state molecular systems. For instance, ultrafast nuclear motions in molecules during chemical reactions have been studied extensively^{15,16,17,18}, enabling the determination of polyatomic molecular structures in electronically excited states^{17,19}. Specific signatures of excited states have also been measured, including the identification of the initially populated electronic state²⁰ and the direct measurement of the redistribution of molecular electron density immediately upon photoexcitation²¹. Further examples of ultrafast gas-phase x-ray scattering measurements include important chemical processes and related properties such as chemical kinetics^{22,23,24}, multiphoton processes^{25,26}, anharmonicities and correlations²⁷.

XX.2. Experimental implementation and data processing

XX.2.1. Experimental implementation

The experimental scheme for ultrafast gas-phase x-ray scattering experiments follows the pump-probe methodology. As illustrated in Fig XX.1, an optical pump laser is used to excite molecules in the gas phase and a subsequent x-ray pulse probes the molecules by casting scattering images on an array detector.



The time delay between the pump and probe pulses is controlled by an electronic delay stage, and the timing jitter is monitored shot-by-shot with a spectrally encoded cross correlator ('time tool') achieving sub-10 fs rms resolution²⁸.

The gas pressure in the sample cell must be carefully adjusted in order to obtain the optimal signal to noise ratio for the pump-probe scattering experiment. The total scattering signal scales linearly with the gas pressure, so that for gas phase structure determination of ground state molecules, higher pressure is always desirable as long as the formation of clusters is avoided. In pump-probe experiments with optical excitation, however, the laser beam can be attenuated by the sample as it traverses the interaction region. If that happens, the scattering signal from downstream molecules does not contain as much pump-probe signal while still contributing to the total scattering signal and therefore to the noise of the measurement. It is not advisable to make up for that by increasing the optical pump pulse energy because that would more likely lead to undesired multi-photon processes. For typical absorption cross sections, the optimum gas pressure is in the range of a few Torr, corresponding to one trillion molecules in the scattering interaction region¹⁴. With about one trillion photons in each x-ray pulse produced at LCLS, only a small fraction ($\approx 10^{-7}$) of the x-ray photons is scattered by the target sample (see Fig XX. 2). As a result, considerable care must be taken to avoid scattering of the primary x-ray beam by any window or air.

The first successful ultrafast gas-phase x-ray scattering experiment studied the ring-opening of CHD¹², and was performed at the x-ray pump-probe (XPP) instrument²⁹ of the linac coherent light source (LCLS). The experiment used a windowless cell for the primary x-ray beam and careful baffling of the background x-rays¹³. More ideally, the imaging detector is enclosed in the vacuum, as is now implemented at the coherent x-ray imaging (CXI) instrument³⁰ at the LCLS. Other improvements in the experimental

implementation include a re-designed short-pathlength windowless scattering cell, careful optimization of the sample density, and normalization of the shot-by-shot x-ray intensity¹⁴, allowing the experiments to achieve an exceptionally high signal-to-noise ratio and sensitivity to very small (~0.1%) changes in the scattering signal. These developments and advances in the experimental methodology are described in a recent methods paper¹⁴.

XX.2.2. Data processing

The measured time-resolved pump-probe scattering signals are conveniently expressed as percent differences^{31,12},

$$\% \Delta I(q, \phi, t) = 100 \frac{I_{\text{on}}(q, \phi, t) - I_{\text{off}}(q, \phi)}{I_{\text{off}}(q, \phi)}, \quad (\text{XX.1})$$

where q is the magnitude of the momentum transfer vector, ϕ the azimuthal angle on the detector, $I_{\text{on}}(q, \phi, t)$ the pump-laser-on scattering signal at delay time t , and $I_{\text{off}}(q, \phi)$ the pump-laser-off reference scattering signal. Using the percent difference expression not only accentuates small changes in the scattering pattern over time but also eliminates many experimental factors that multiplicatively affect both laser-on and laser-off scattering signals. These factors, which include pixel noise, attenuation of the scattered signal by the beryllium exit window, scattering intensity corrections due to the linear polarization of the x-rays at LCLS (x-ray polarization factor), and the detector planarity (geometric correction factor), are discussed in section 2.4 of reference¹⁴.

It is important to note that there are several other experimental artifacts that do not cancel out when using the percent differences. This includes the shot-by-shot x-ray intensity fluctuations of the self-amplified spontaneous emission (SASE) pulses at non-seeded XFELs. To take this factor into account, the transmitted x-ray intensity after the gas sample is monitored by a photodiode mounted downstream of the detector. The x-ray scattering signals are then corrected using the measured photodiode value shot-by-shot *before* averaging. In addition, any experimental uncertainties introduced by the pump laser such as laser intensity fluctuations and changes in the laser/x-ray spatial overlap remain and must be handled carefully. Finally, even though background scattering from apparatus components is eliminated in the numerator of equation XX.1, it still remains in the denominator and therefore needs to be minimized. It has been shown that the current experimental design assisted by careful data processing can yield exceptionally high quality data with experimental backgrounds at least three orders smaller than the desired scattering signal¹⁴.

In order to measure the scattering patterns as a function of q and ϕ accurately, it is important to calibrate the detector geometry with regards to factors such as the position of the detector center and the sample-to-detector distance. A least-squares optimization between the two-dimensional theoretical reference image generated from a calculated ground-state molecular geometry and the experimentally

measured laser-off scattering pattern, $I_{\text{off}}(q, \phi)$, is performed for this purpose. To directly compare the measured absolute scattering signals with the theoretical ones, the aforementioned factors including the x-ray polarization and the geometric correction factors, which are eliminated in the percent difference signal (eq. XX.1), must now be included. The calibration procedure optimizes parameters that define the center of the detector, the azimuthal angle of the detector relative to the x-ray polarization direction, and the distance of the detector relative to the interaction region.

XX.3. Observing excited-state molecular systems in real time

Excited-state molecular systems usually display a complex interplay between the electron density distributions and the nuclei^{32,33}. In the Born-Oppenheimer approximation, the electrons create a potential energy landscape that guides the trajectory of nuclei, while the electron density itself evolves as the nuclei move along the potential energy surface during the chemical reaction. The Born-Oppenheimer approximation breaks down in the vicinity of conical intersections where two or more potential energy surfaces of equal symmetry intersect, strongly coupling the electronic and nuclear motions. The determination of nuclear motions and the rearrangement of electron density distributions is thus essential for understanding excited state chemical reactions and processes. With the capability to observe both nuclear and electron dynamics in molecules, time-resolved x-ray scattering offers unique views that are complementary to spectroscopic methods. In this section, we describe various important new insights and observables for excited-state molecular systems that have been unveiled by state-of-the-art ultrafast gas-phase x-ray scattering experiments.

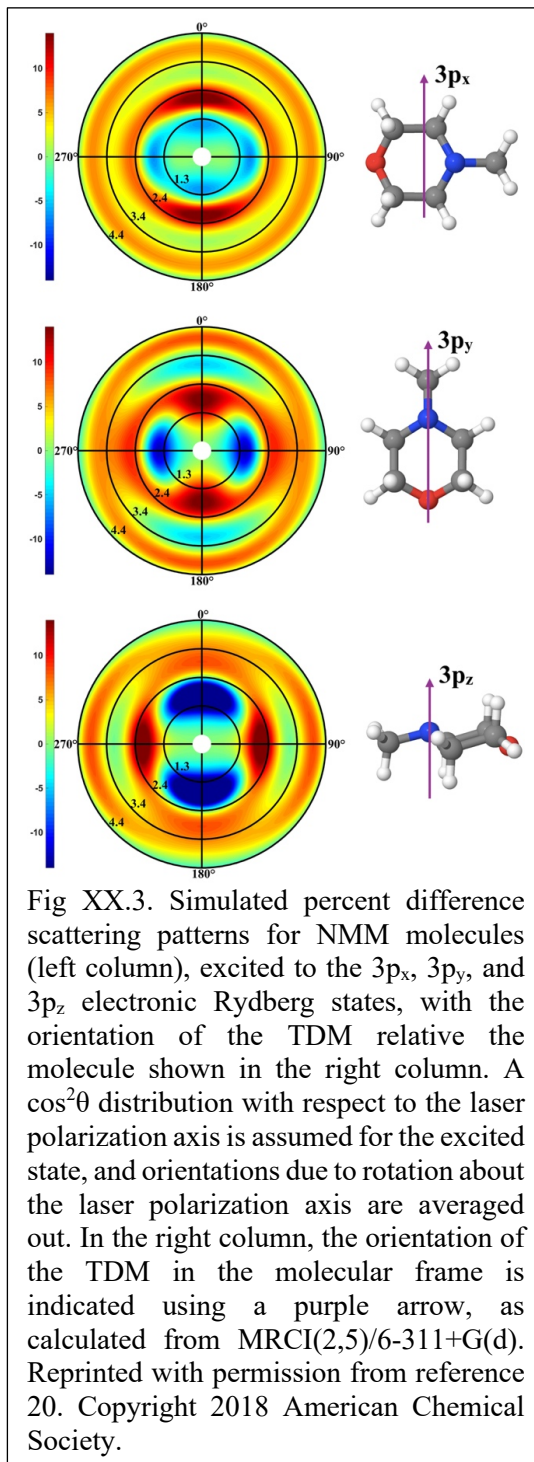


Fig XX.3. Simulated percent difference scattering patterns for NMM molecules (left column), excited to the $3p_x$, $3p_y$, and $3p_z$ electronic Rydberg states, with the orientation of the TDM relative the molecule shown in the right column. A $\cos^2\theta$ distribution with respect to the laser polarization axis is assumed for the excited state, and orientations due to rotation about the laser polarization axis are averaged out. In the right column, the orientation of the TDM in the molecular frame is indicated using a purple arrow, as calculated from MRCI(2,5)/6-311+G(d). Reprinted with permission from reference 20. Copyright 2018 American Chemical Society.

XX.3.1. Transition dipoles and multi-photon processes with anisotropic x-ray scattering

The time-energy uncertainty relationship implies that molecular absorption that induces the ultrafast excited state dynamics is inherently broad. Consequently, traditional spectroscopic investigations often remain ambiguous even about which specific excited state is initially populated. A direct measurement of the optical transition dipole moment can therefore provide essential guidance for successful analysis.

It is known from both theoretical predictions^{34,35} and experimental measurements^{36,37} that gas-phase x-ray scattering from aligned molecules can have angle-dependent scattering patterns due to the intrinsic anisotropy of the molecular geometry. However, for an ensemble of free molecules with random orientations, the x-ray scattering patterns are isotropic (other than the polarization factor) and can be conveniently analyzed using rotationally averaged scattering signals. Due to various limitations of molecular alignment techniques and complexities associated with introducing a third alignment laser^{36,37}, almost all pump-probe gas-phase x-ray scattering experiments to date start with randomly orientated molecules.

Nevertheless, the pump-probe x-ray scattering patterns from isotropic ensembles of free molecules

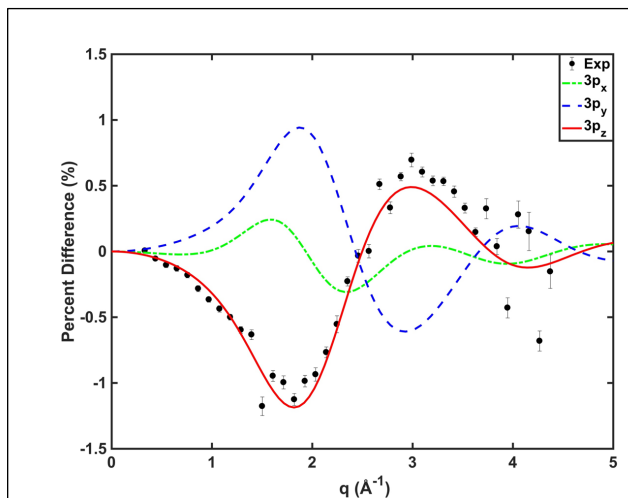


Fig XX.4. Anisotropic signal derived from experimental results at a pump-probe delay time of $t = 150$ fs. The three theoretical signals are derived from the calculated results shown in Fig XX.2. Reprinted with permission from reference 20. Copyright 2018 American Chemical Society.

can be anisotropic^{16,20}. As illustrated in the insets of Fig XX.1, the angle-dependent signal usually appears at very early delay times (≈ 200 fs) before quickly disappearing thereafter (≈ 1 ps), even though it sometimes reappears at much longer delay times (≈ 4 ps). This effect is caused by the interaction of the linearly polarized optical light with the gas-phase ensemble and subsequent rotational motions of the molecule in the laboratory frame^{38,39}. Because the optical pump laser is linearly polarized, those molecules whose transition dipole moment vector (TDM) aligns with the polarization of the laser pump pulse in the laboratory frame will be preferentially excited. This

creates a molecular ensemble with an anisotropic population of excited-state molecules as well as an anisotropic population of unexcited ground-state molecules, leading to angle-dependent scattering signals. Subsequent rotational dephasing and rephasing of the molecules after photoexcitation are responsible for the disappearance and recurrence of the anisotropic scattering signal. In general, such anisotropic scattering signals can be conveniently decomposed with $2n$ order Legendre polynomials for an n -photon absorption process. The zeroth order term, called isotropic term, contains all the information in the molecular frame

that can be simplified as the isotropic rotationally averaged signal, while additional information about the transition dipole moment²⁰ and multi-photon processes²⁶ can be extracted from higher-order, anisotropic terms.

The orientation of the optical TDM can be determined using the anisotropic component of ultrafast pump-probe x-ray scattering signals, allowing for the identification of the initially excited electronic state prepared by the optical excitation²⁰. The concept is illustrated in Fig XX.3 for N-methyl morpholine (NMM) molecules. Single-photon excitation with a pulsed 200 nm laser can, at least in principle, excite any one or a mixture of the three energetically close 3p Rydberg states. As simulated in Fig XX.3, the resulting pump-probe percent difference scattering patterns are markedly different for the three TDM orientations that correspond to the three 3p states. This is because the intrinsic orientation of the TDM in the molecular frame determines the orientations of the excited-state population of molecules in the laboratory frame, which is then reflected in the angular-dependence of the scattering signal. By comparing the simulated 2-dimensional patterns in Fig XX.3 with the experimental results in Fig XX.1, it is straightforward to see that only the simulated pattern for 3p_z excitation shows the same symmetry as the experiment. To quantitatively compare the results, the 2nd order Legendre polynomial term, which represents the anisotropic scattering components, is extracted from the original two-dimensional scattering pattern. As is evident from Fig XX.4, the result unambiguously determines that the optical excitation is predominantly to the 3p_z state, with almost no admixture of the other two states.

For multi-photon excitations, the anisotropy of ultrafast x-ray scattering signals has been used by Natan *et al.* to resolve and disentangle different multiphoton processes in a single experiment²⁶. They show the decomposed experimental anisotropy terms up to order $n=10$ in the Legendre polynomial for gas-phase I₂ molecules excited by 520 nm laser pulses, with noticeable signals up to the $n=8$ term. This suggests that multi-photon processes up to 4-photon absorption are taking place for iodine when interacting with a 520 nm, high intensity optical pulse ($\sim 5 \times 10^{11}$ W/cm²). One should note that an anisotropic scattering signal from a n^{th} order term also has projections to all $k < n$ order Legendre polynomials. However, by analyzing all higher order terms, different reaction channels that are excited by different multiphoton transitions can be filtered out. The anisotropy information can thus be used as a powerful toolbox to differentiate and trace multiple excitation pathways that occur simultaneously.

XX.3.2. Excited-state electron densities in real space

The first step in all photochemical and photophysical processes, photoexcitation, has conventionally been studied using spectroscopic tools which measure the transitions between different states^{40,41,42}. It has been proposed theoretically that pump-probe scattering experiments have the potential

to image the dynamic changes in the electron density upon photoexcitation^{34,43,44,45,46}. The first direct experimental observation of the initial redistribution of electron density in a molecule upon photoexcitation was recently achieved using ultrafast gas-phase x-ray scattering²¹.

Fig XX.5 shows the direct measurement of the initial redistribution of electron density when the molecule 1,3-cyclohexadiene (CHD) is optically excited to an electronic 3p Rydberg state by a 200 nm pump pulse²¹. The difference radial distribution function shown in Fig XX.5a, $\Delta\text{RDF}(r)$, is obtained from the experimental difference signal via a sine transform. It shows, in real space, the rapid redistribution of the electron density at ~ 25 fs after photoexcitation. The depletion of the electron density at small distances (0-3 Å) and the broad increase at larger distances (4-9 Å) reflects the diffuse character of the 3p Rydberg state and matches well with theoretically calculated electron density differences as illustrated in the inset of Fig XX.5a. In Fig XX.5b, comparison between experimental and theoretical percent difference scattering signals shows good agreement, providing further evidence that the changes in electron density due to transitions between electronic states are clearly observed.

The experiment introduced here is aided by the fact that the CHD is a relatively small organic molecule without heavy elements, that the 3p state of CHD has a relatively long lifetime (~ 200 fs)^{47,23}, and that the change in the electronic structure of the 3p Rydberg state is large while the changes in molecular geometry are small. With the ongoing improvements in XFEL sources⁴⁸ and developments of scattering theories for data analysis^{49,50,51}, it can be

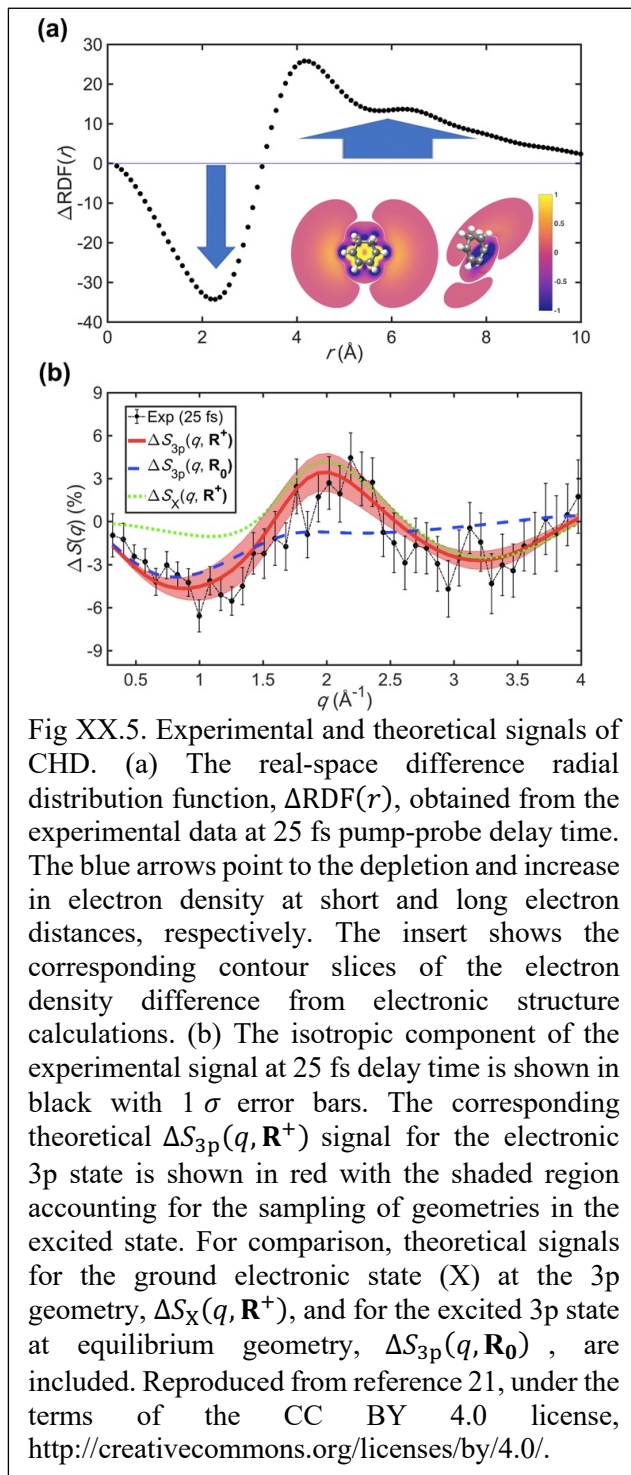
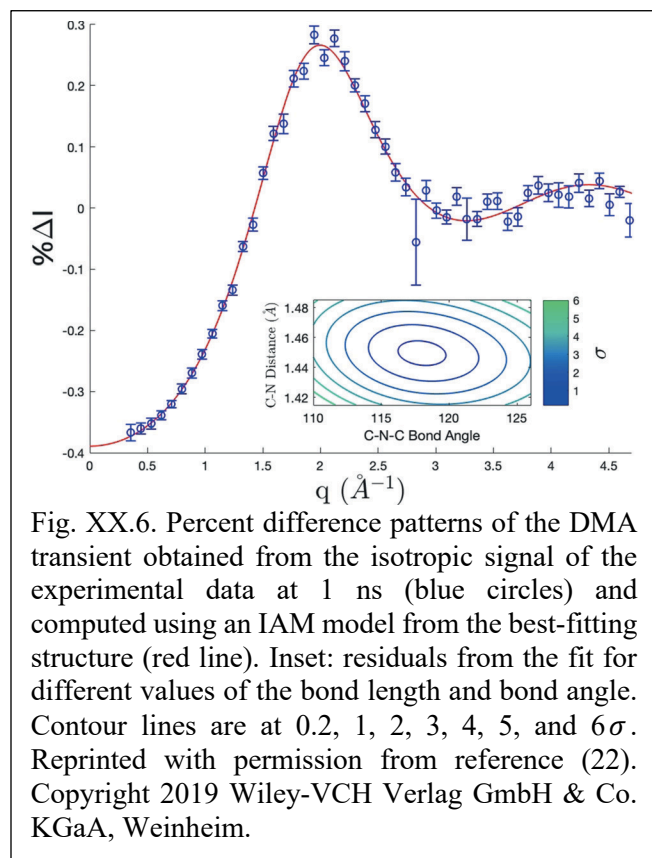


Fig XX.5. Experimental and theoretical signals of CHD. (a) The real-space difference radial distribution function, $\Delta\text{RDF}(r)$, obtained from the experimental data at 25 fs pump-probe delay time. The blue arrows point to the depletion and increase in electron density at short and long electron distances, respectively. The insert shows the corresponding contour slices of the electron density difference from electronic structure calculations. (b) The isotropic component of the experimental signal at 25 fs delay time is shown in black with 1σ error bars. The corresponding theoretical $\Delta S_{3p}(q, \mathbf{R}^+)$ signal for the electronic 3p state is shown in red with the shaded region accounting for the sampling of geometries in the excited state. For comparison, theoretical signals for the ground electronic state (X) at the 3p geometry, $\Delta S_X(q, \mathbf{R}^+)$, and for the excited 3p state at equilibrium geometry, $\Delta S_{3p}(q, \mathbf{R}_0)$, are included. Reproduced from reference 21, under the terms of the CC BY 4.0 license, <http://creativecommons.org/licenses/by/4.0/>.

expected for ultrafast x-ray scattering to measure electron density distributions in valence excited states and to image time-evolving electron dynamics in the near future.

XX.3.3. Determination of excited-state molecular geometry

The determination of excited state molecular geometries from the direct inversion of scattering patterns is challenging because of the fundamental phase problem⁵² in all x-ray scattering techniques including x-ray crystallography, because of the limited range of the scattering momentum transfer vectors observed in the experiment, and, depending on circumstances, because the geometry may be undefined for instance due to strong dispersion of the wavepacket (see e.g. ref. 53). For gas-phase scattering experiments, the problem is further compounded by the rotational averaging due to randomly oriented molecules in the sample and the intrinsic structural complexity of polyatomic molecules. Following the procedures of



conventional gas phase diffraction experiments⁵⁴, one therefore compares experimental scattering patterns with calculated patterns and deems the molecular structure to be determined when satisfactory agreement is reached. We note that only the intensity information of scattered x-rays is used in the analysis of current ultrafast x-ray scattering experiments. It has been shown that the phase information in diffraction patterns of a virus can be measured through techniques like x-ray Fourier holography imaging⁵⁵. It might be possible to extend such techniques to the molecular scale.

XX.3.3.1. Least-squares refinement

Traditionally, a least-squares refinement of structural parameters is used to determine molecular structures from scattering data⁵⁴. Based

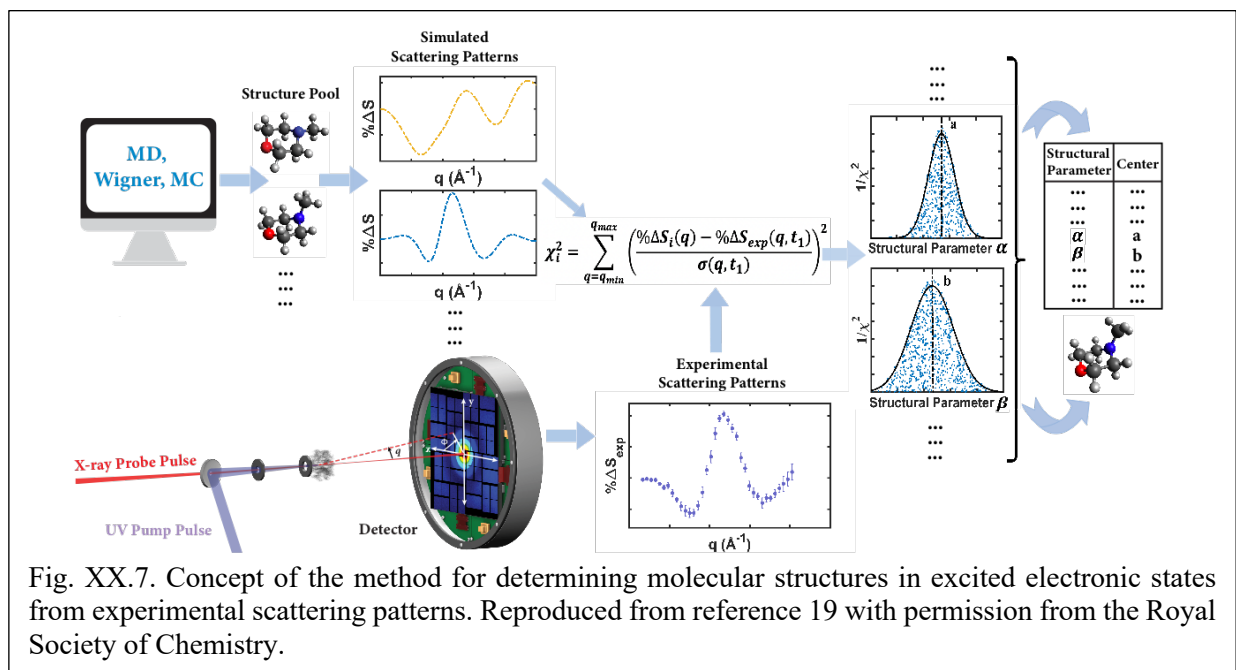
on a hypothetical structure, a matrix of interatomic distances R_{ij} is constructed for the molecules in their ground electronic states. Then, the independent atom model (IAM, see [Scattering theory section](#)) is invoked to calculate scattering patterns from interatomic distance matrix. A least-squares refinement of selected adjustable parameters, such as a set of bond lengths and angles, is performed to retrieve best-fitting structural parameters by minimizing the difference between calculated and experimental scattering signals.

This method works well also for transient species created by optical excitation to a dissociative state, provided that the fragments are in their ground electronic state and have only a few degrees of freedom, or when only specific coordinates are of interest^{56,22}. This concept has been adopted to determine the structure of transient dimethylamine radical (DMA) measured by ultrafast gas-phase x-ray scattering²², Fig XX.6. Keeping the C-H distances in DMA fixed, the fits yield the precise DMA structure with a C-N-C bond angle of $118 \pm 4^\circ$ and a C-N bond length of $1.45 \pm 0.02 \text{ \AA}$.

XX.3.3.2. Structure pool analysis

For complicated polyatomic molecules, the least-squares refinement approach becomes difficult and almost impossible to implement. The choice of the independent adjustable parameters becomes problematic for nonlinear molecules with more than 4 atoms, because an N -atomic nonlinear molecule has $\frac{N(N-1)}{2}$ interatomic distances while only $3N - 6$ geometrical parameters are needed. As the number of atom-atoms distances scales with N^2 while the number of geometrical parameters scales linearly with N , there are correlations between structural parameters chosen for refinement that can cause multiple solutions and possibly unphysical structures. The correlation problem becomes more pronounced for molecular systems that are far from their equilibrium²⁷, such as molecules in excited electronic states. To circumvent this complexity, a novel structure determination method has been developed^{19,17} that is capable of determining precise excited-state molecular structures of polyatomic molecules with more than 4 non-hydrogenic atoms^{17,24}.

The concept of the method is illustrated in Fig. XX.7. The method compares the experimentally measured scattering patterns against the simulated patterns corresponding to a large pool of molecular



structures to determine the full set of structural parameters. It consists of three important steps¹⁹: *creating a structure pool*, *calculating scattering patterns* and *determining molecular structures*.

Creating a structure pool. The first step is to create a pool of trial structures that are in the vicinity of the target structure in the large conformation space. It has been found that one million trial structures are enough to reach the convergence for molecular systems like NMM (15 degrees of freedom excluding hydrogen atoms)¹⁷. A larger number of structures would be necessary for molecular systems with more degrees of freedom. Three sampling methods for creating structure pools have been introduced¹⁹, including molecular dynamics sampling (MD pool), Wigner sampling (Wigner pool) and Monte Carlo based sampling (MC pool). The MD pool is created by calculating molecular dynamics trajectories that propagate on potential surfaces that resemble the subject of the study. The structures in the pool are extracted from MD trajectories without reference to their time sequence. As the ultimate goal of the structure pool is to provide many structure that are in the vicinity of the correct target structure, one could sample many physically viable structures by displacing their geometries so as to provide the opportunity to find unexpected structures. This can be done either by sampling geometries from a Wigner distribution⁵⁷ (Wigner pool), or by using a Monte Carlo based approach to randomly create chemically viable structures (MC pool). Further details of the three sampling methods can be found in the section 2.2.1 of the reference 19. In principle, the method for creating the structure pool is not limited to the three methods introduced here, as the concept in Fig. XX.7 itself is largely independent of the method employed as long as the created pool is sufficiently expansive in the vicinity of the sought structure and dense enough to yield good matches to the experimental patterns. The choice of the sampling method is thus partially a matter of convenience and should depend on the experiment at hand. For example, because the MD pool samples structures across a large section of the available geometries, it is particularly useful when the studied molecular systems involve a coherent dynamic motion through a significant part of the potential energy surface¹⁷. However as the MD simulation itself is comparatively computationally expensive, the Wigner and MC pools are better choices when the target system is an equilibrium excited-state structure that is near the minimum of a potential surface^{19,24}.

Calculating scattering patterns. With the structure pool at hand, a simulated scattering pattern needs to be calculated for every structure in the pool. The theoretical percent difference scattering signal of an excited-state molecular system can be written as²¹

$$\% \Delta S_{\text{exc}}(q, \mathbf{R}') = 100 \frac{I_{\text{exc}}^{\text{vib}}(q, \mathbf{R}') - I_{\text{X}}(q, \mathbf{R}_0)}{I_{\text{X}}(q, \mathbf{R}_0)}, \quad (\text{XX.2})$$

where $I_{\text{exc}}^{\text{vib}}(q, \mathbf{R}')$ is the excited-state scattering intensity including vibrational excitation and $I_{\text{X}}(q, \mathbf{R}_0)$ is the scattering intensity of the ground-state molecule, with \mathbf{R}' and \mathbf{R}_0 the equilibrium nuclear geometries of the excited state and the ground-state molecule, respectively. The theoretical percent difference signal can

be directly related to the experimental percent difference signal (eq. XX.1) by $\% \Delta I = \gamma \% \Delta S_{\text{exc}}$, where γ is the fraction of molecules that are optically excited, a scalar quantity that can be determined from the experimental analysis. It has been shown previously^{19,21} that by inserting two null contributions, $0 = I_X^{\text{vib}}(q, \mathbf{R}') - I_X^{\text{vib}}(q, \mathbf{R}')$ and $0 = I_X(q, \mathbf{R}') - I_X(q, \mathbf{R}')$, eq. XX.2 can be rewritten as

$$\begin{aligned} \% \Delta S_{\text{exc}}(q, \mathbf{R}') &= 100 \cdot \left(\frac{I_{\text{exc}}^{\text{vib}}(q, \mathbf{R}') - I_X^{\text{vib}}(q, \mathbf{R}')}{I_X(q, \mathbf{R}_0)} + \frac{I_X^{\text{vib}}(q, \mathbf{R}') - I_X(q, \mathbf{R}')}{I_X(q, \mathbf{R}_0)} + \frac{I_X(q, \mathbf{R}') - I_X(q, \mathbf{R}_0)}{I_X(q, \mathbf{R}_0)} \right) \\ &= \Delta S^{\text{elec}}(q, \mathbf{R}') + \Delta S_{\text{vib}}^{\text{nucl}}(q, \mathbf{R}') + \Delta S_0^{\text{nucl}}(q, \mathbf{R}'), \end{aligned} \quad (\text{XX.3})$$

where $\Delta S^{\text{elec}}(q, \mathbf{R}')$ represents the electronic contribution, i.e. the difference between the excited and ground electronic state scattering signal at the molecular geometry \mathbf{R}' , assuming that the electronic excitation does not affect the molecular vibrations. The term $\Delta S_{\text{vib}}^{\text{nucl}}(q, \mathbf{R}')$ describes the contribution from the change in molecular vibrations upon laser excitation at a given structure \mathbf{R}' , and, finally, $\Delta S_0^{\text{nucl}}(q, \mathbf{R}')$ accounts for change in scattering signal that stems solely from the change in molecular geometry from \mathbf{R}_0 to \mathbf{R}' while remaining on the ground electronic state.

In principle, the structure determination method introduced in Fig. XX.7 can be implemented with any choice of method to calculate the scattering patterns and to construct the theoretical percent difference scattering signals. For example, an *ab initio* calculation can be adopted to directly calculate the x-ray scattering terms $I_{\text{exc}}^{\text{vib}}(q, \mathbf{R}')$ and $I_X(q, \mathbf{R}_0)$ that are required for Eq. XX.2^{34,50,58}. Unfortunately the *ab initio* calculations are computationally expensive and almost impossible to be implemented for a large structure pool with more than one million structures. With the ongoing developments of computationally efficient

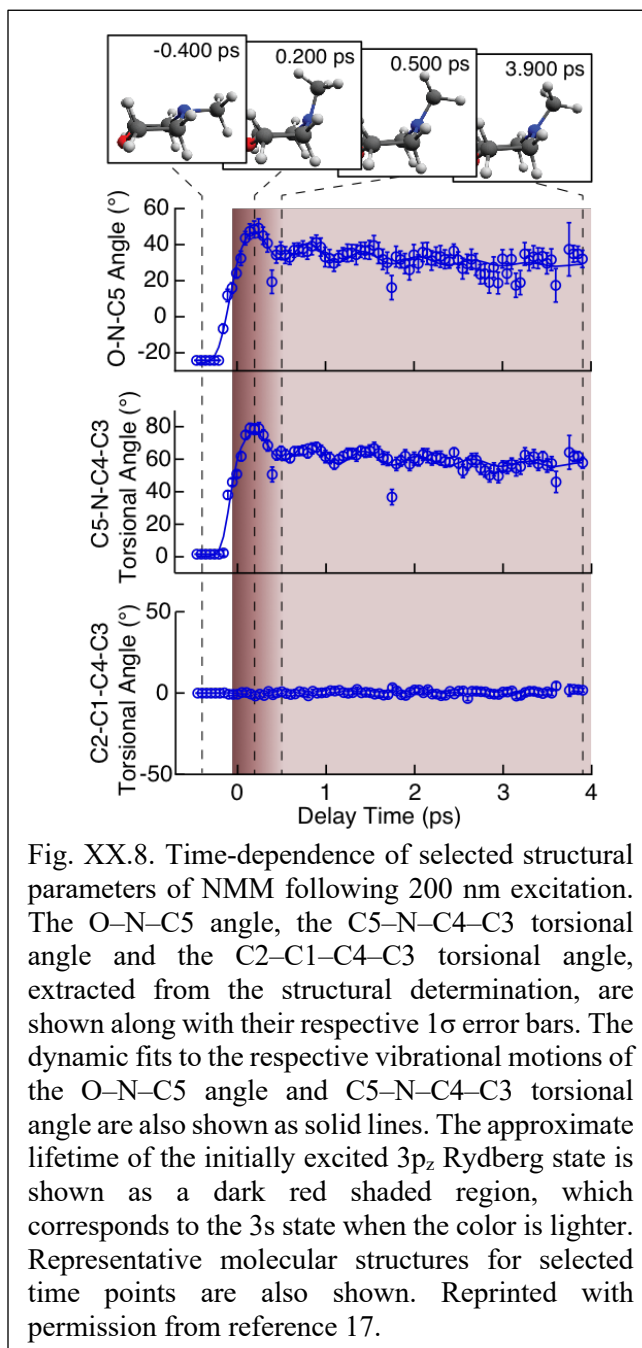


Fig. XX.8. Time-dependence of selected structural parameters of NMM following 200 nm excitation. The O–N–C5 angle, the C5–N–C4–C3 torsional angle and the C2–C1–C4–C3 torsional angle, extracted from the structural determination, are shown along with their respective 1σ error bars. The dynamic fits to the respective vibrational motions of the O–N–C5 angle and C5–N–C4–C3 torsional angle are also shown as solid lines. The approximate lifetime of the initially excited $3p_z$ Rydberg state is shown as a dark red shaded region, which corresponds to the $3s$ state when the color is lighter. Representative molecular structures for selected time points are also shown. Reprinted with permission from reference 17.

methods for predicting the scattering patterns^{46,59,60}, this current computational bottlenecks could be addressed in the near future.

Eq. XX.3 can be adopted instead to circumvent the current complexity. Previous studies have shown that the $\Delta S^{\text{elec}}(q, \mathbf{R}')$ term for electronic excitation to a Rydberg state is observable and nearly independent of the molecular geometry for reasonably small variations in the structure²¹. This suggests that the $\Delta S^{\text{elec}}(q, \mathbf{R}')$ term can be treated as a constant correction term¹⁷ that can be simulated accurately with high level *ab initio* x-ray scattering calculations, while the time-dependent scattering signal is mainly attributed to the change of the nuclear geometry, $\Delta S_0^{\text{nucl}}(q, \mathbf{R}')$. The IAM can adequately describe the $\Delta S_0^{\text{nucl}}(q, \mathbf{R}')$ term despite being a rather crude approximation, in part due to the strongly bound core electrons. While neglecting the specific effects of any distortion in the valence electron density distribution, it nicely captures the scattering difference caused by changing molecular geometry and avoids potential systematic errors that might be introduced by inaccuracies of *ab initio* electronic structure methods. Additionally, the IAM offers computational simplicity and efficiency so that it can easily be applied to a large pool of structures. The influence of vibrational state distributions, $\Delta S_{\text{vib}}^{\text{nucl}}(q, \mathbf{R}')$, has been found to be negligible within the current experimental range of scattering vectors and a detection limit of $\sim 0.05\%$, even when the molecules are assumed to have a comparatively high internal vibrational energy¹⁹. Nevertheless, Eq. XX.3 offers a means to include the effects of changes in the vibrational distribution, once this becomes observable with further improvements in the experimental technique.

Determining molecular structures. The last step is to determine molecular structures from experimental patterns. For each calculated theoretical percent difference scattering pattern from the structure pool, the χ^2 deviation from the experimental pattern is calculated as¹⁹

$$\chi_i^2 = \sum_{q=q_{\min}}^{q_{\max}} \left(\frac{\% \Delta S_i(q) - \% \Delta S_{\text{exp}}(q, t_1)}{\sigma(q, t_1)} \right)^2 \quad (\text{XX.4})$$

where $\% \Delta S_i(q)$ is the computed percent difference pattern for structure i in the pool, $\% \Delta S_{\text{exp}}(q, t_1)$ is the experimental percent difference scattering pattern $\% \Delta I(q, t)$ divided by the excitation fraction γ at delay time t_1 , and $\sigma(q, t_1)$ represents the experimental uncertainty of $\% \Delta S_{\text{exp}}(q, t_1)$, calculated as the statistical counting noise. Each structure in the pool is associated with a specific χ_i^2 value calculated by Eq. XX.4, representing how well the structure's scattering pattern agrees with the experimentally measured pattern. To determine the best structure, the inverse of the χ_i^2 values, i.e. χ_i^{-2} , are plotted against molecular structure parameters such as the interatomic distances, bond angles or torsional angles, for all structures. By looking at the complete distributions instead of just picking the lowest χ_i^2 structures, artifacts associated with the sparse sampling can be largely overcome. Given the randomness inherent in the generation of the structure pools, it is not surprising that for any value of a structure parameter, there are many structures that give

poor fits, i.e. high values of χ_i^2 as sketched in Fig. XX.7 for structural parameters α and β . Those poor fits fall beneath the envelope of the overall distribution. Retaining only the best-fitting structure for each value of the structure parameter, the envelope of the distribution assumes a normal or skewed normal distribution¹⁷. The maxima of the envelope is then taken as the determined value for each structural parameter, and a complete set of structural parameters can be constructed as the determined molecular structure. One should note that the functional form for describing the envelope of the χ_i^{-2} distribution and the bin widths of structural parameters should be carefully chosen, as has been discussed in detail in reference¹⁹.

Conceptually, the plot of χ_i^{-2} is a surface in a multi-dimensional space, as it depends on the $3N - 6$ dimensions for a non-linear molecule with N atoms. The best-fitting structure should be the extremal point on this surface. Because it is impractical to simulate the entire multi-dimensional space, it is reduced to a series of one-dimensional fits that can be viewed as projections of the multi-dimensional surface onto a specific structural parameter. One should note that a list of determined structural parameters does not necessarily correspond to a physically possible structure because of correlations between structural parameters⁶¹. For the method described in this section, the correlations between structural parameters have been shown to be largely preserved, since each χ_i^{-2} value shown in the plot is calculated from a *physically possible* 3D geometrical structure¹⁹. Beside overcoming the problem of correlations among different structural parameters of the molecule, the structure pool analysis has two further advantages compared to a traditional least-squares refinement approach. First, it prevents the analysis from converging to a structure that is physically or chemically impossible. Second, the analysis does not require assumptions regarding the molecular symmetry, making it applicable to relatively complicated polyatomic molecular systems. For example, the method has been utilized to record an experimental “molecular movie” uncovering the coherent vibrational motions in excited-state NMM¹⁷. The full time-dependent structural parameters of NMM from 0 to 4 ps were determined, with several selected representative structural parameters of NMM as a function of time shown in Fig. XX.8. This study also determined the equilibrium structure of NMM in the excited 3s electronic state after the damping of the coherent vibrations^{17,19}, with a precision in the parameters on the order of 0.01 Å.

XX.3.3.3. Weighted molecular dynamics trajectories

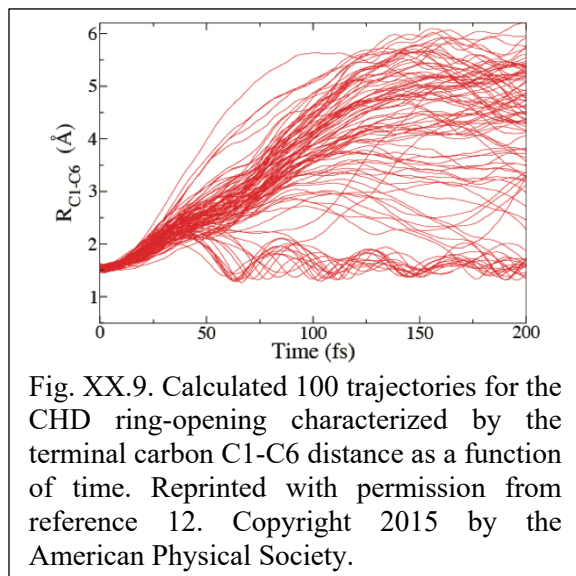
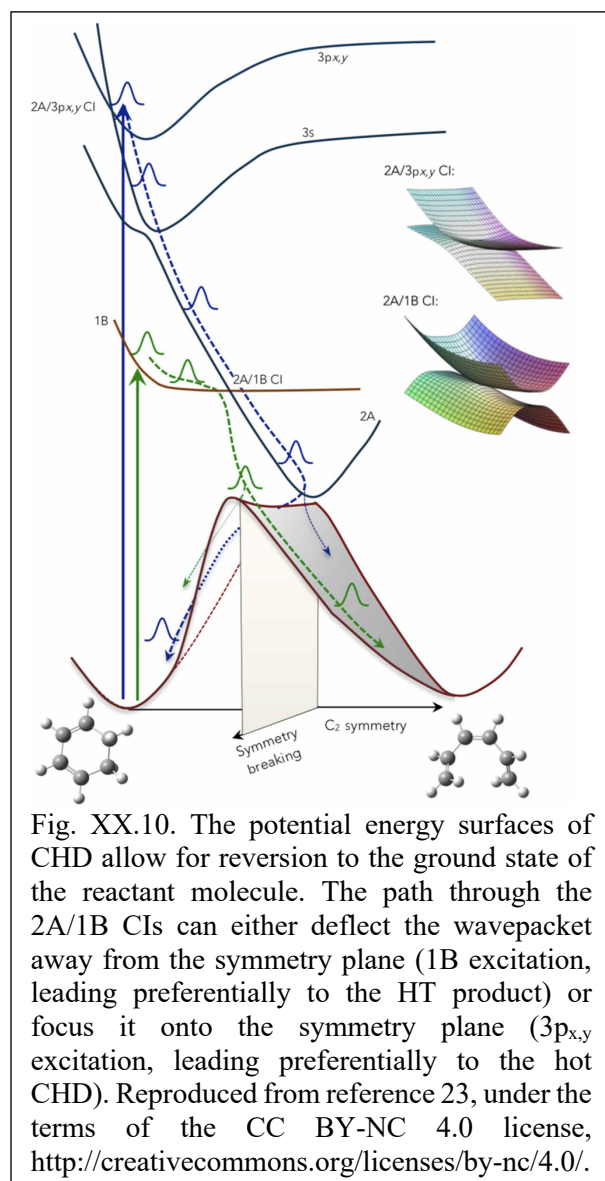


Fig. XX.9. Calculated 100 trajectories for the CHD ring-opening characterized by the terminal carbon C1-C6 distance as a function of time. Reprinted with permission from reference 12. Copyright 2015 by the American Physical Society.



The structure pool analysis method can be applied to time-dependent dynamics problems, although in implementations to date each time point is analyzed individually for the molecular structure. Dynamic molecular structures evolve continuously, so that structures at neighboring time points must be related, provided the time points are finely enough spaced. The 2015 study of the ring-opening dynamics of CHD explicitly takes this into account¹². About 100 quantum molecular dynamics trajectories (shown in Fig. XX.9) were calculated using the multiconfigurational Ehrenfest method⁶² with potential energies and nonadiabatic couplings obtained on-the-fly at the SA3-CAS(6,4)/cc-pVDZ level of theory. All trajectories were compared with the time-dependent experimental data, resulting in a weight for each trajectory that was determined from a multi-start nonlinear least-square optimization routine with a finite-difference gradient¹². The overall distribution of weighted trajectories represents the shape of the wavepacket and determines the associated structures for each individual species at any given time delay.

XX.3.4. Ultrafast chemical reaction dynamics

The first gas-phase x-ray scattering study of chemical reaction dynamics with femtosecond time resolution explored the ring-opening dynamics of CHD with 267 nm excitation¹². Illustrated by a green arrow in Fig. XX.10, optical excitation at 267 nm prepares the molecule in the 1B valence state. The wavepacket slides down the 1B potential energy surface and transitions through two conical intersections (CI) to the ground state of the ring-open 1,3,5-hexatriene (HT) product⁶³. Interestingly, a 200 nm excitation of CHD to the 3p state results in a different reaction pathway, leading to a kinetic ring-opening reaction on the ground electronic surface that will be discussed in the next section²³.

The dynamic ring-opening reaction of CHD, a prototypical example of an electrocyclic reaction, has been studied extensively by spectroscopic experiments^{64,65,66}. Even though the time scales were well

known, the time-evolving molecular structures during the reaction remained experimentally undetermined. By using ultrafast x-ray scattering, the molecular motions associated with the ring-opening reaction of CHD became accessible. Fig. XX.11 shows ultrafast x-ray scattering patterns of CHD at several selected time points. To model the dynamic motions of the molecule, the 100 calculated trajectories of Fig. XX.9 were weighted and compared to the experimental signals using the method described in the section XX.3.3.3. As shown in Fig. XX.11, the fits (colored lines) agree well with the experimental data (black lines). From the analysis, the time-dependent molecular structures of both ring-opening and ring-closed channels are extracted, with a branching ratio determined as 3:2, i.e. 60% HT yield¹². A later theoretical study⁶⁷ using extended multistate complete active space second-order perturbation (XMS-CASPT2) surface hopping found a quantum yield for HT formation to be $47 \pm 8\%$, which is in reasonable agreement with the ultrafast x-ray scattering study.

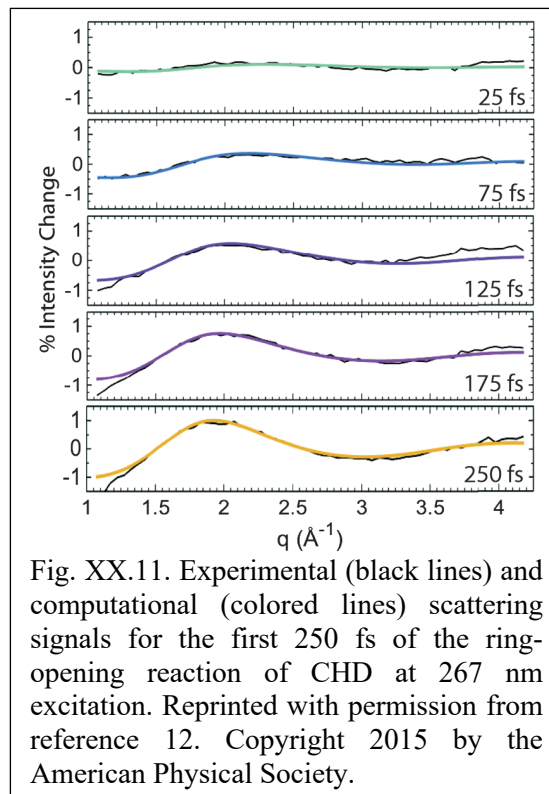


Fig. XX.11. Experimental (black lines) and computational (colored lines) scattering signals for the first 250 fs of the ring-opening reaction of CHD at 267 nm excitation. Reprinted with permission from reference 12. Copyright 2015 by the American Physical Society.

For simple molecular systems, specifically diatomic molecules such as I_2 , frequency-resolved x-ray scattering signals obtained from the temporal Fourier transform of the time-resolved x-ray scattering

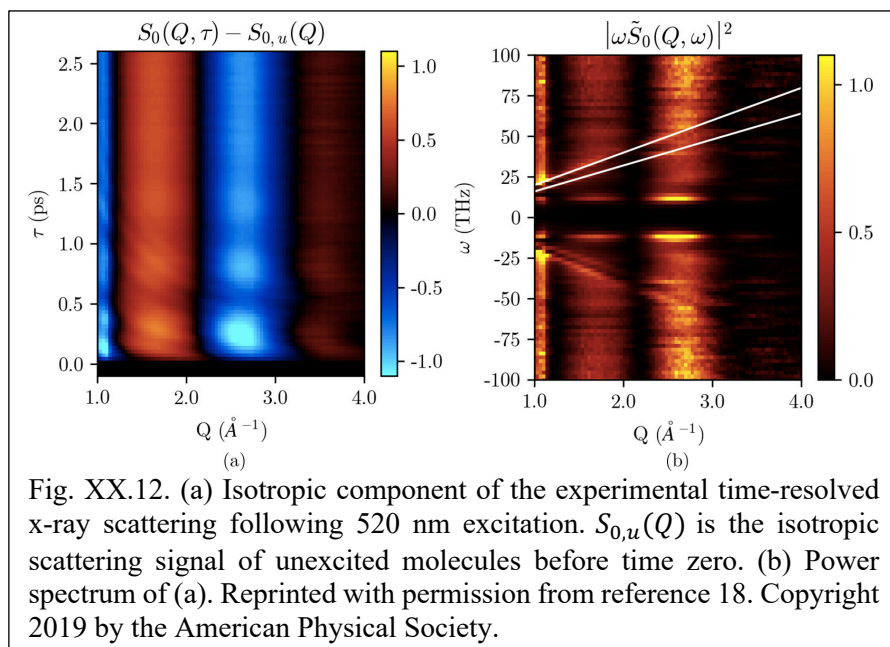


Fig. XX.12. (a) Isotropic component of the experimental time-resolved x-ray scattering following 520 nm excitation. $S_{0,u}(Q)$ is the isotropic scattering signal of unexcited molecules before time zero. (b) Power spectrum of (a). Reprinted with permission from reference 18. Copyright 2019 by the American Physical Society.

patterns can be used to characterize bound and dissociative motions of the molecule¹⁸. Fig. XX.12 shows the ultrafast x-ray scattering signal of I_2 in both time domain and frequency domain. There are two dissociation channels indicated as white lines, with positive slopes in the positive angular frequency region. The final

velocities for the two dissociations were determined to be $16.4 \pm 0.2 \text{ \AA/ps}$ and $19.9 \pm 0.2 \text{ \AA/ps}$, respectively. There is also a bound state motion peaked at $\omega = 11.6 \pm 1.1 \text{ THz}$, which is shown as a bright horizontal line in the positive angular frequency region. Frequency-resolved x-ray scattering provides a useful interpretation of the ultrafast x-ray scattering signal for diatomic systems. Implementations for more complex polyatomic molecules, and in molecular systems with multiple competing dissociation pathways, remain to be developed⁶⁸.

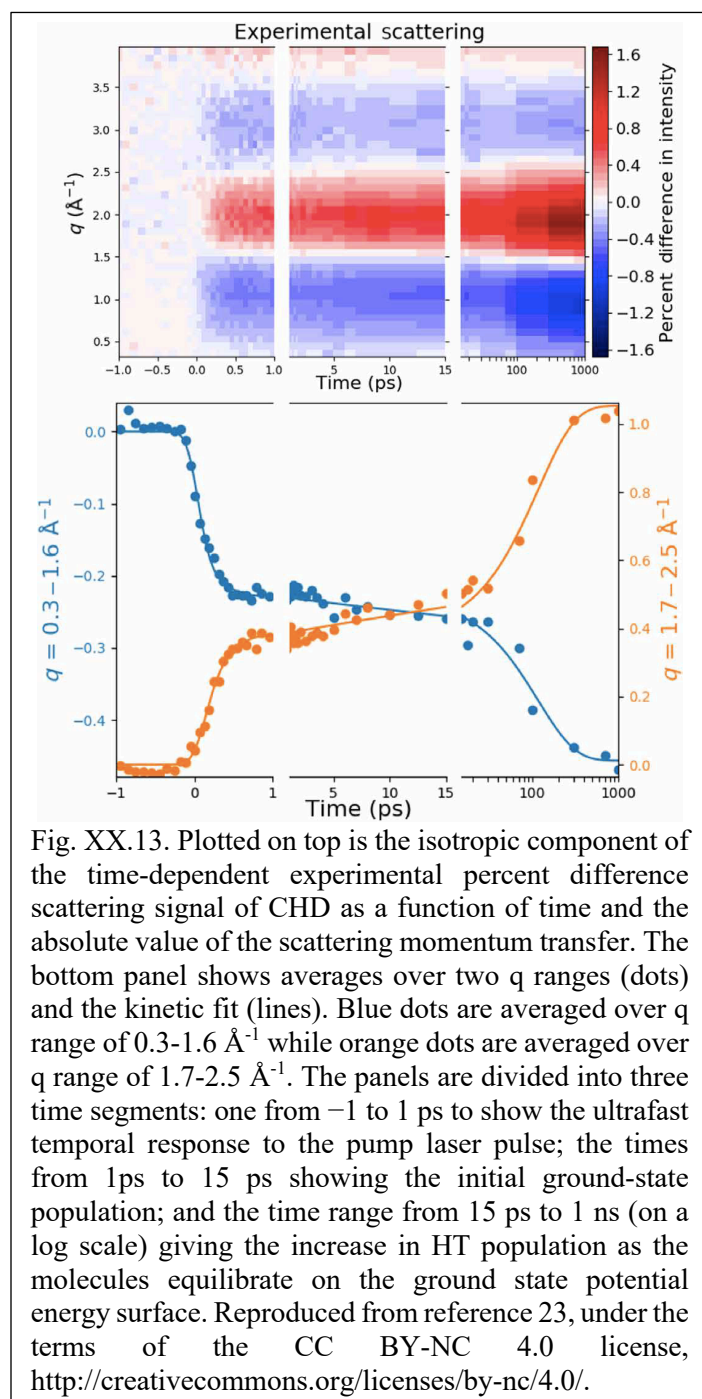


Fig. XX.13. Plotted on top is the isotropic component of the time-dependent experimental percent difference scattering signal of CHD as a function of time and the absolute value of the scattering momentum transfer. The bottom panel shows averages over two q ranges (dots) and the kinetic fit (lines). Blue dots are averaged over q range of $0.3\text{-}1.6 \text{ \AA}^{-1}$ while orange dots are averaged over q range of $1.7\text{-}2.5 \text{ \AA}^{-1}$. The panels are divided into three time segments: one from -1 to 1 ps to show the ultrafast temporal response to the pump laser pulse; the times from 1 ps to 15 ps showing the initial ground-state population; and the time range from 15 ps to 1 ns (on a log scale) giving the increase in HT population as the molecules equilibrate on the ground state potential energy surface. Reproduced from reference 23, under the terms of the CC BY-NC 4.0 license, <http://creativecommons.org/licenses/by-nc/4.0/>.

XX.3.5. Ultrafast chemical kinetics

Dynamic motions of molecules as discussed above entail the movements of wavepackets across potential energy surfaces that are concerted across all molecules of an ensemble. Kinetic reactions occur when the wavepackets have dephased and the reaction dynamics is better described using statistical models. In kinetic reactions, only the reactants, any transients and the reaction products are observed while the passing through transition states remains obscured. Nevertheless, a great deal of information can be obtained by studying chemical kinetics on ultrafast time scales. Time-dependent x-ray scattering patterns measured from femtosecond to picosecond or further to nanosecond time scales have been applied to study the kinetics of photoinduced chemical reactions^{22,23,24}. Because chemical kinetics can usually be modeled with rate equations, the time-dependent scattering signals can be viewed as orthogonal contributions with the time dependence following the kinetic process and the q dependence arising from the patterns of the individual transient

species. The time-dependent x-ray scattering signal can then be modeled as^{23,24}

$$\% \Delta I_{iso}(q, t) = \gamma (\sum_{\alpha} \% \Delta S_{\alpha}(q) F_{\alpha}(t)) * g(t), \quad (\text{XX.5})$$

where $\% \Delta I_{iso}(q, t)$ is the isotropic component of the $\% \Delta I(q, \phi, t)$, $\% \Delta S_{\alpha}(q)$ represents the isotropic percent difference scattering pattern of transient structure α , which can be treated as adjustable parameters, while $F_{\alpha}(t)$ is the corresponding time-dependent population as determined by the kinetics scheme. The

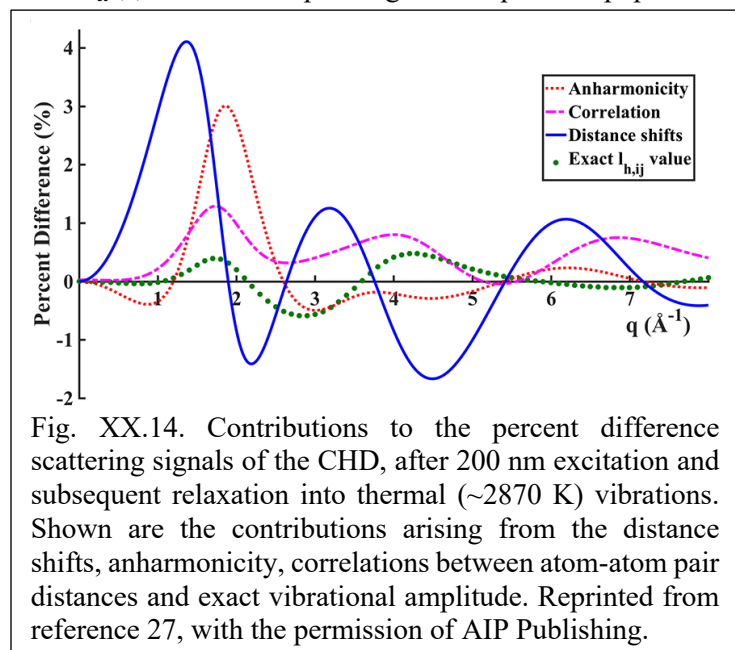


Fig. XX.14. Contributions to the percent difference scattering signals of the CHD, after 200 nm excitation and subsequent relaxation into thermal (~ 2870 K) vibrations. Shown are the contributions arising from the distance shifts, anharmonicity, correlations between atom-atom pair distances and exact vibrational amplitude. Reprinted from reference 27, with the permission of AIP Publishing.

scalar γ is the excitation probability and $g(t)$ is a Gaussian function that characterizes the temporal instrument response. By fitting the experimental data using eq. XX.5, the time constants of the kinetic scheme and the scattering patterns, $\% \Delta S_{\alpha}(q)$, of individual transient species can be determined simultaneously from a global fit. This concept has been used to study the photoinduced ground-state ring-opening kinetics of CHD²³ and the intramolecular excited state charge transfer of N,N'-dimethylpiperazine²⁴.

While excitation of the CHD molecule at 266 nm results in dynamic motions, excitation at 200 nm, which leads to the 3p Rydberg state, results in an electronically excited state with a short, but measurable lifetime. Fig. XX.13 shows the experimental results of CHD upon excitation to the 3p state²³. In addition to the initially excited state and the subsequent electronic decay on the femtosecond time scale, the experimental data shows a gradually evolving signal from picosecond regime up to 1 ns. This suggests that a kinetic reaction on the hot ground state of the system is involved following the electronic decay of the initially excited 3p state. By using eq. XX.5 to fit the experimental data, a full reaction scheme of the kinetics can be unveiled as illustrated in Fig. XX.10. The analysis determined that the initially excited 3p state decays in 208 ± 11 fs to the electronic ground state. During this process, $76 \pm 3\%$ of the molecules were found to decay back to the vibrationally hot, ring-closed ground-state CHD, while the remainder undergoes a rapid ring-opening reaction to form hot HT. A thermal ring-opening reaction on the ground electronic state surface then occurs and an equilibrium between the

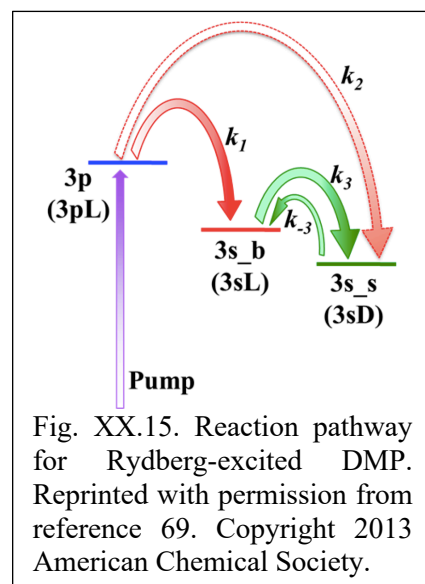


Fig. XX.15. Reaction pathway for Rydberg-excited DMP. Reprinted with permission from reference 69. Copyright 2013 American Chemical Society.

hot CHD and hot HT is reached with the ring-opening and ring-closing time constants determined to be 174 ± 13 ps and 355 ± 45 ps, respectively. The analysis also yields the scattering patterns of the separate hot CHD and HT products. To accurately model the scattering patterns of the hot products, a novel method based on molecular dynamics trajectories was developed²⁷. As shown in Fig. XX.14, this is necessary for vibrationally hot molecules because large amplitude vibrational motions are usually anharmonic, and correlated distances and distance shifts must be included when modeling their scattering patterns.

In N,N'-dimethylpiperazine (DMP), previous photoelectron investigations have shown that excitation to the 3p state will lead to rapid relaxation to the charge-localized (3sL) and charge-delocalized (3sD) conformers in the 3s state on the femtosecond time scale. As shown in Fig. XX.15, the charge transfer then proceeds as the molecules evolve on the 3s potential energy surface. An equilibrium between 3sL and 3sD conformers is reached with an overall time constant of 2.65 ps⁶⁹. This kinetic scheme was recently confirmed by an ultrafast x-ray scattering experiment²⁴. Using the previously determined reaction kinetics and eq. XX.5, the scattering patterns of the 3sL and 3sD products were extracted as shown in Fig. XX.16. By using the structure determination method based on structure pools as described in section XX.3.3.2, complete molecular structures of the charge-localized and the charge-delocalized species in the 3s state were determined. It was found that charge transfer weakens the carbon-carbon bond to an unusual 1.634 Å bond length while the bond lengths between the nitrogen and the ring-carbon atoms contract from an average of 1.505 to 1.465 Å²⁴. This demonstrates that the ultrafast x-ray scattering can resolve the changes in molecular structure that arise from charge transfer and can provide valuable benchmarks for the evaluation of computational electronic structure methods^{70,71}.

XX.4. Summary

The advent of XFEL facilities has had a transformative impact on the study of excited-state molecular structure and chemical reaction dynamics. One of the experimental techniques enabled by XFELs is ultrafast time-resolved gas-phase x-ray scattering. Accurate

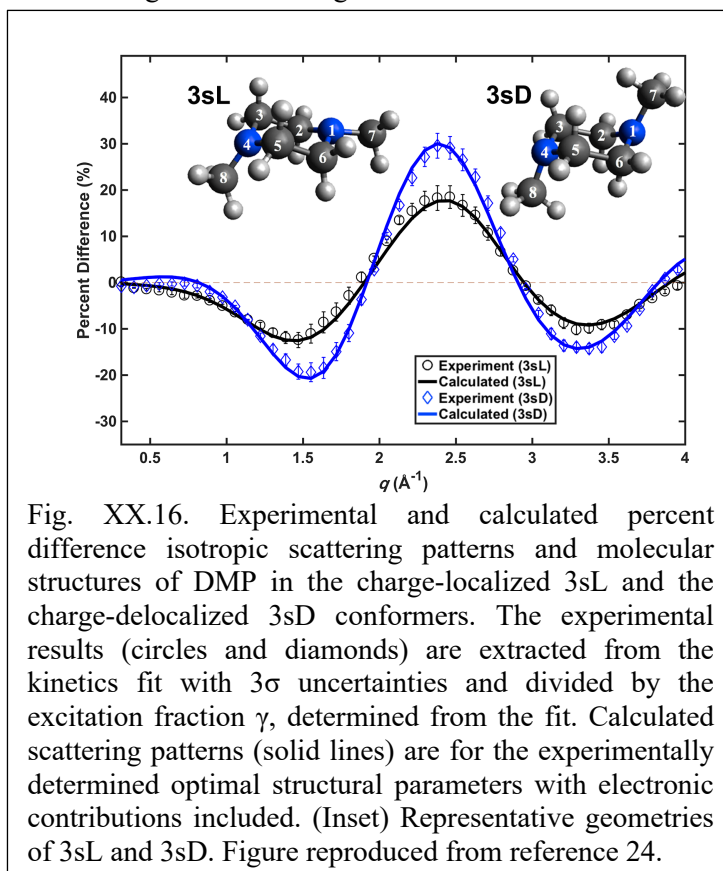


Fig. XX.16. Experimental and calculated percent difference isotropic scattering patterns and molecular structures of DMP in the charge-localized 3sL and the charge-delocalized 3sD conformers. The experimental results (circles and diamonds) are extracted from the kinetics fit with 3σ uncertainties and divided by the excitation fraction γ , determined from the fit. Calculated scattering patterns (solid lines) are for the experimentally determined optimal structural parameters with electronic contributions included. (Inset) Representative geometries of 3sL and 3sD. Figure reproduced from reference 24.

measurements of excited state electron densities and molecular geometries provide new insights into chemical bonding and molecular dynamics, and offer essential benchmarks for the further development of theory and computational methods in dynamics and electronic structure theory. Ultrafast time-resolved, gas-phase x-ray scattering is capable of resolving both nuclear and electron motions during chemical reactions. Further advances, including higher energy photons and high repetition rate XFELs such as LCLS-II⁴⁸, the ongoing development of ultrafast x-ray scattering theory^{72,49,51,73,74} and advanced structural inversion methods^{75,76,77} promise future ultrafast x-ray scattering experiments that directly map the coupled electron and nuclear motions, providing a detailed and comprehensive view of chemical reactions in real time^{78,79}.

Acknowledgements

The research of PMW and his group benefited from funding by the U.S. Department of Energy, Office of Science, Basic Energy Sciences, award # DE-SC0017995 and DE-SC0020276, and from the National Science Foundation, award # CHE-1953839. In addition, AK acknowledges funding from the Engineering and Physical Sciences Research Council (EP/V049240/1 and EP/V006819/1), the Leverhulme Trust (RPG-2020-208), and a natural sciences fellowship at the Swedish Collegium for Advanced Study with financial support from the Erling-Persson Family Foundation and the Knut and Alice Wallenberg Foundation.

References

1. Ischenko AA, Weber PM, Miller RJD, *Chem Rev*, 2017, **117**, 11066.
2. Emma P, Akre R, Arthur J, Bionta R, Bostedt C, Bozek J et al., *Nat Photon*, 2010, **4**, 641.
3. Decking W, Abeghyan S, Abramian P, Abramsky A, Aguirre A, Albrecht C et al., *Nat Photon*, 2020, **14**, 391.
4. Serrano-Andres L, Serrano-Perez JJ, In: Leszczynski J, editor. *Handbook of computational chemistry*, Springer, Dordrecht, 2012.
5. Spence JCH, *Struct Dyn*, 2017, **4**, 044027.
6. Stefanou M, Saita K, Shalashilin DV, Kirrander A, *Chem Phys Lett*, 2017, **683**, 300.
7. Ma L, Yong H, Geiser JD, Moreno Carrascosa A, Goff N, Weber PM, *Struct Dyn*, 2020, **7**, 034102.
8. Rouxel JR, Keefer D, Mukamel S, *Struct Dyn*, 2021, **8**, 014101.
9. Bargheer M, Zhavoronkov N, Woerner M, Elsaesser T, *ChemPhysChem*, 2006, **7**, 783.
10. Ihee I, Lorenc M, Kim TK, Kong QY, Cammarata M, Lee JH et al., *Science*, 2005, **309**, 1223.
11. Warren, BE, *X-Ray Diffraction*, Addison-Wesley, New York, 1968.
12. Minitti MP, Budarz JM, Kirrander A, Robinson JS, Ratner D, Lane TJ et al., *Phys Rev Lett*, 2015, **114**, 255501.
13. Budarz JM, Minitti MP, Cofer-Shabica DV, Stankus B, Kirrander A, Hastings JB et al., *J Phys B: At Mol Opt Phys*, 2016, **49**, 034001.

-
14. Stankus B, Yong H, Ruddock JM, Ma L, Moreno Carrascosa A, Goff N et al., *J Phys B: At Mol Opt Phys*, 2020, **53**, 234004.
 15. Stankus B, Budarz JM, Kirrander A, Rogers D, Robinson J, Lane TJ et al., *Faraday Discuss*, 2016, **194**, 525.
 16. Glowonia JM, Natan A, Cryan JP, Hartsock R, Kozina M, Minitti MP et al., *Phys Rev Lett*, 2016, **117**, 153003.
 17. Stankus B, Yong H, Zotev N, Ruddock JM, Bellshaw D, Lane TJ et al., *Nat Chem*, 2019, **11**, 716.
 18. Ware MR, Glowonia JM, Al-Sayyad N, O'Neal JT, Bucksbaum PH, *Phys Rev A*, 2019, **100**, 033413.
 19. Yong H, Moreno Carrascosa A, Ma L, Stankus B, Minitti MP, Kirrander A et al, *Faraday Discuss*, 2021, **228**, 104.
 20. Yong H, Zotev N, Stankus B, Ruddock JM, Bellshaw D, Boutet S et al., *J Phys Chem Lett*, 2018, **9**, 6556.
 21. Yong H, Zotev N, Ruddock JM, Stankus B, Simmermacher M, Moreno Carrascosa A et al., *Nat Commun*, 2020, **11**, 2157.
 22. Ruddock JM, Zotev N, Stankus B, Yong H, Bellshaw D, Boutet S et al., *Angew Chem Int Ed*, 2019, **58**, 6371.
 23. Ruddock JM, Yong H, Stankus B, Du W, Goff N, Chang Y et al., *Sci Adv*, 2019, **5**, eaax6625.
 24. Yong H, Xu X, Ruddock JM, Stankus B, Moreno Carrascosa A, Zotev N et al., *Proc Natl Acad Sci U.S.A.*, 2021, **118**, e2021714118.
 25. Bucksbaum PH, Ware MR, Natan A, Cryan JP, Glowonia JM, *Phys Rev X*, 2020, **10**, 011065.
 26. Natan A, Schori A, Owolabi G, Cryan JP, Glowonia JM, Bucksbaum PH, *Faraday Discuss*, 2021, **228**, 123.
 27. Yong H, Ruddock JM, Stankus B, Ma L, Du W, Goff N et al., *J Chem Phys*, 2019, **151**, 084301.
 28. Bionta MR, Hartmann N, Weaver M, French D, Nicholson DJ, Cryan JP et al., *Rev Sci Instrum*, 2014, **85**, 083116.
 29. Chollet M, Alonso-Mori R, Cammarata M, Damiani D, Defever J, Delor JT et al., *J Synchrotron Rad*, 2015, **22**, 503.
 30. Liang M, Williams GJ, Messerschmidt M, Seibert MM, Montanez PA, Hayes M et al., *J Synchrotron Rad*, 2015, **22**, 514.
 31. Dudek RC, Weber PM, *J Phys Chem A*, 2001, **105**, 4167.
 32. Yarkony DR, *Rev Mod Phys*, 1996, **68**, 985.
 33. Butler LJ, *Annu Rev Phys Chem*, 1998, **49**, 125.
 34. Northey T, Zotev N, Kirrander A, *J Chem Theory Comput*, 2014, **10**, 4911.
 35. Moreno Carrascosa A, Northey T, Kirrander A, *Phys Chem Chem Phys*, 2017, **19**, 7853.
 36. Küpper J, Stern S, Holmegaard L, Filsinger F, Rouzée A, Rudenko A et al, *Phys Rev Lett*, 2014, **112**, 083002.
 37. Kierspel T, Morgan A, Wiese J, Mullins T, Aquila A, Barty A et al., *J Chem Phys*, 2020, **152**, 084307.
 38. Felker PM, Zewail AH, *J Chem Phys*, 1987, **86**, 2460.
 39. Felker PM, *J Phys Chem*, 1992, **96**, 7844.
 40. Geßner O, Lee AMD, Shaffer JP, Reisler H, Levchenko SV, Krylov AI et al., *Science*, 2006, **311**, 219.
 41. Li W, Jaroń-Becker AA, Hogle CW, Sharma V, Zhou X, Becker A et al., *Proc Natl Acad Sci U.S.A.*, 2010, **107**, 20219.

-
42. Attar AR, Bhattacharjee A, Pemmaraju CD, Schnorr K, Closser KD, Prendergast D et al., *Science*, 2017, **356**, 54.
 43. Ben-Nun M, Martínez TJ, Weber PM, Wilson KR, *Chem Phys Lett*, 1996, **262**, 405.
 44. Debnarova A, Techert S, Schmatz S, *J Chem Phys*, 2010, **133**, 124309.
 45. Kirrander A, *J Chem Phys*, 2012, **137**, 154310.
 46. Parrish RM, Martínez TJ, *J Chem Theory Comput*, 2019, **15**, 1523.
 47. Bühler CC, Minitti MP, Deb S, Bao J, Weber PM, *J Atom Mol Phys*, 2011, **2011**, 637593.
 48. Halavanau A, Decker FJ, Emma C, Sheppard J, Pellegrini C, *J Synchrotron Radiat*, 2019, **26**, 635.
 49. Bennett K, Kowalewski M, Rouxel JR, Mukamel S, *Proc Natl Acad Sci U.S.A.*, 2018, **115**, 6538.
 50. Carrascosa AM, Yong H, Crittenden DL, Weber PM, Kirrander A, *J Chem Theory Comput*, 2019, **15**, 2836.
 51. Simmermacher M, Moreno Carrascosa A, Henriksen NE, Møller KB, Kirrander A, *J Chem Phys*, 2019, **151**, 174302.
 52. Taylor G, *Acta Cryst*, 2003, **D59**, 1881.
 53. Makhija V, Boguslavskiy AE, Forbes R, Veyrinas K, Wilkinson I, Lausten R et al., *Faraday Discuss*, 2021, **228**, 191.
 54. Hargittai I, In: Hargittai I, Hargittai M, editor, *Stereochemical applications of gas-phase electron diffraction*, Wiley-VCH, Weinheim, 1st ed., 1988.
 55. Gorkhover T, Ulmer A, Ferguson K, Bucher M, Maia FRNC, Bielecki J et al., *Nat Photon*, 2018, **12**, 150.
 56. Yang J, Guehr M, Shen X, Li R, Vecchione T, Coffee R et al., *Phys Rev Lett*, 2016, **117**, 153002.
 57. Dahl JP, Springborg M, *J Chem Phys*, 1988, **88**, 4535.
 58. Northey T, Moreno Carrascosa A, Schafer S, Kirrander A, *J Chem Phys*, 2016, **145**, 154304.
 59. Northey T, Kirrander A, *J Phys Chem A*, 2019, **123**, 3395.
 60. Zotev N, Moreno Carrascosa A, Simmermacher M, Kirrander A, *J Chem Theory Comput*, 2020, **16**, 2594.
 61. Havel TF, In: Schleyer PR, Allinger NL, Clark T, Gasteiger J, Kollman PA, Schaefer HF, Schreiner PR, editor. *Encyclopedia of computational chemistry*, John Wiley and Sons, Ltd., 2002.
 62. Saita K, Shalashilin DV, *J Chem Phys*, 2012, **137**, 22A506.
 63. Deb S, Weber PM, *Annu Rev Phys Chem*, 2011, **62**, 19.
 64. Garavelli M, Page CS, Celani P, Olivucci M, Schmid WE, Trushin SA et al., *J Phys Chem A*, 2001, **105**, 4458.
 65. Kuthirummal N, Rudakov FM, Evans CL, Weber PM, *J Chem Phys*, 2006, **125**, 133307.
 66. Pemberton CC, Zhang Y, Saita K, Kirrander A, Weber PM, *J Phys Chem A*, 2015, **119**, 8832.
 67. Polyak I, Hutton L, Crespo-Otero R, Barbatti M, Knowles PJ, *J Chem Theory Comput*, 2019, **15**, 3929.
 68. Gabalski I, Ware MR, Bucksbaum PH, *J Phys B: At Mol Opt Phys*, 2020, **53**, 244002.
 69. Deb S, Cheng X, Weber PM, *J Phys Chem Lett*, 2013, **4**, 2780.
 70. Cheng X, Zhang Y, Jónsson E, Jónsson H, Weber PM, *Nat Commun*, 2016, **7**, 11013.
 71. Gałynska M, Ásgeirsson V, Jónsson H, Björnsson R, Localized and delocalized states of a diamine cation: A critical test of wave function methods. arXiv [Preprint] (2020). <https://arxiv.org/pdf/2007.06125> (Accessed 15 July 2020).

-
72. Dixit G, Vendrell O, Santra R, *Proc Natl Acad Sci U.S.A.*, 2012, **109**, 11636.
73. Moreno Carrascosa A, Yang M, Yong H, Ma L, Kirrander A, Weber PM et al., *Faraday Discuss*, 2021, **228**, 60.
74. Yong H, Keefer D, Mukamel S, *J Am Chem Soc*, 2022, **144**, 7796.
75. Asenov M, Zotev N, Ramamoorthy S, Kirrander A. Inversion of ultrafast x-ray scattering with dynamics constraints. In *Machine Learning and the Physical Sciences*, 7. Vancouver, Canada, 2020.
<https://ml4physicalsciences.github.io/2020/>.
76. Zhang M, Zhang S, Xiong Y, Zhang H, Ischenko AA, Vendrell O et al., *Nat Commun*, 2021, **12**, 5441.
77. Hosseinizadeh A, Breckwoldt N, Fung R, Sepehr R, Schmidt M, Schwander P et al., *Nature*, 2021, **599**, 697.
78. Simmermacher M, Henriksen NE, Möller KB, Moreno Carrascosa A, Kirrander A, *Phys Rev Lett*, 2019, **122**, 073003.
79. Keefer D, Aleotti F, Rouxel JR, Segatta F, Gu B, Nenov A et al., *Proc Natl Acad Sci U.S.A.*, 2021, **118**, e2022037118.